European Journal of Mechanics / A Solids 118 (2026) 106130

Contents lists available at ScienceDirect

European Journal of Mechanics / A Solids

journal homepage: www.elsevier.com/locate/ejmsol

Full Length Article

Influence of material and geometrical parameters on the adhesive performance of vibration-modulated soft contacts

M. Tricarico [a], A.Y. Shiferaw [a], A. Papangelo [a,b,*]

[a] Politecnico di Bari, Department of Mechanics Mathematics and Management, TriboDynamics Lab, Via Orabona 4, Bari, 70125, Italy
[b] Hamburg University of Technology, Department of Mechanical Engineering, Am Schwarzenberg-Campus 1, Hamburg, 21073, Germany

A B S T R A C T

Vibroadhesion, the modulation of interfacial adhesion by superimposing small-amplitude, high-frequency vibrations on an adhesive contact, offers a simple and fast strategy to rapidly tune contact forces. A systematic understanding of how key geometrical and material parameters govern this behavior is still lacking. Here, we present a comprehensive experimental investigation of vibroadhesion in viscoelastic PDMS–glass Hertzian contacts, examining the influence of substrate thickness t, radius of the indenter R, material properties like modulus and thermodynamic surface energy, unloading rate r and preload F_{c0} on the stickiness performance of vibration-modulated interfaces such as: pull-off force F_{PO}, contact radius a, mean stress at pull-off σ_{PO}, maximum enhancement with respect to the static adhesion test, range of vibration amplitudes that sustain adhesion enhancement. We find that across all tests, vibration activation triggers an abrupt expansion of the contact area, which upon unloading, results in a substantial increase of the pull-off force up to a saturation level always coinciding with the vibration level causing interfacial instabilities at the interface (wrinkles). Although the absolute value of the pull-off force may be strongly influenced by geometrical and material parameters, the maximum adhesion enhancement with respect to the reference static test remained consistently close to a 13-fold increase. We obtained the maximum mean stress at pull-off of 186 kPa when indenting with the smallest sphere. The unloading rate r weakly affects the adhesive performance and the preload F_{c0} is nearly irrelevant in determining the pull-off force F_{PO}. Taken together, these results provide both physical insights and practical guidelines for designing vibration-modulated adhesive interfaces for rapid, reversible, and tunable adhesion.

1. Introduction

Controlled modulation of adhesion in soft interfaces is valuable for gripping (Shintake et al., 2018), bio-integrated devices (Bae et al., 2013), and reversible attachment (Liu and Yan, 2022; Duan et al., 2023; Tan et al., 2024). Over the past decades, several approaches have been proposed to design and tune adhesion properties, such as bioinspired surface patterning (Hensel et al., 2018; Greiner et al., 2009; Zhang et al., 2022; Peisker et al., 2013; Carbone et al., 2011), actuation via mechanical forces (Wang et al., 2022; Johannes et al., 2022), electric (Caruso et al., 2025) and magnetic (Zhao et al., 2022; Drotlef et al., 2014) fields, temperature (Linghu et al., 2024, 2025), light (Liu et al., 2023), pH (Narkar et al., 2019) and pneumatic systems (Tang et al., 2025).

Besides the many strategies cited above, superimposing small, high-frequency normal oscillations on an otherwise quasi-static contact has recently emerged as a remarkably simple and fast way to increase or decrease adhesion on demand. In their seminal experiments, Shui et al. (2020) conducted indentation tests using a rigid borosilicate glass lens (radius of curvature $R = 51.5$ mm) suspended by a rubber band brought in contact with a vibrating 3 mm-thick PolyDiMethylSiloxane (PDMS) layer. Vibration frequencies and amplitudes were varied in the ranges of 100–800 Hz and 0–160 μm, respectively. For the first time, Shui et al. (2020) demonstrated that tuning the amplitude and frequency of normal vibrations produced changes in interfacial adhesion strength (i.e., pull-off force) ranging from complete suppression of adhesion to a 78-fold enhancement with respect to the static (without vibration) indentation test establishing the basic phenomenology of what we here refer to as vibroadhesion. Very importantly, the switching timescale from high to weak adhesion was of the order of tens milliseconds, a response time comparable to geckos (Autumn and Peattie, 2002).

The physical mechanism underlying vibroadhesion is viscoelastic adhesion hysteresis. In fact, a soft contact can be described as an external crack propagating or healing at the interface, which leads to viscoelastic dissipation of energy, ultimately resulting in rate-dependent adhesion (Persson and Brener, 2005; Maghami et al., 2024a; Wang et al., 2025; Schapery, 1975; Greenwood and Johnson, 1981; Afferrante and Violano, 2022; Violano and Afferrante, 2022; Violano et al., 2021). As a consequence, the effective (or apparent) work of adhesion $\Delta\gamma_{eff}$ depends on the crack speed $v = -da/dt$ (i.e., the rate at which the contact radius

* Corresponding author. Politecnico di Bari, Department of Mechanics Mathematics and Management, TriboDynamics Lab, Via Orabona 4, Bari, 70125, Italy.
E-mail address: antonio.papangelo@poliba.it (A. Papangelo).

https://doi.org/10.1016/j.euromechsol.2026.106130
Received 7 February 2026; Received in revised form 25 March 2026; Accepted 30 March 2026
Available online 1 April 2026

a decreases as the interface separates, in analogy with crack propagation in fracture mechanics): it decreases upon crack closure and increases upon crack opening with respect to the thermodynamic work of adhesion $\Delta\gamma_0$ (which is an interfacial property), in accordance with the well-established semi-empirical model proposed by Gent and Schultz (1972):

$$\Delta\gamma_{eff} = \begin{cases} \Delta\gamma_0\left(1+\left|\frac{v}{v_0}\right|^{\alpha}\right), v \geq 0, \text{(opening crack)} \\ \Delta\gamma_0\left(1+\left|\frac{v}{v_0}\right|^{\alpha}\right)^{-1}, v < 0, \text{(closing crack)} \end{cases} \quad (1)$$

where v is the crack speed and $\{v_0, \alpha\}$ are the Gent-Schultz constants, with v_0 a reference crack velocity and α the power-law exponent. For broad-band materials, like PDMS 10:1 base to crosslink weight ratio, α is about ~ 0.2 (Maghami et al., 2024b). This asymmetry results in a hysteresis loop when the viscoelastic interface is cyclically loaded and unloaded within the vibration period leading to a dynamic modulation of the effective surface energy (Tricarico et al., 2025; Yi et al., 2024).

More recently, Tricarico et al. (2025) employed a setup similar to that of Shui et al. (2020), confirming the main findings but noticing that the adhesion enhancement, defined as the ratio between the pull-off force F_{PO} obtained under vibration and the "reference" value F^0_{PO} obtained under a static test (without vibration), strongly depends on how the "reference pull-off" F^0_{PO} is chosen. Shui et al. (2020) defined F^0_{PO} as obtained unloading the spherical indenter after it had gently touched the soft PDMS layer resulting in an almost vanishing preload F_{c0}. Nevertheless, it is well known that in adhesive indentation tests the pull-off force increases with the preload and then saturates. For this reason, Tricarico et al. (2025) increased the preload up to the condition it did not affect the pull-off force resulting in a minimum preload of $|F_{c0}| = 250$ mN. In the following we will refer to the latter procedure to determine the reference pull-off force F^0_{PO}. Tricarico et al. (2025) showed that when unloading in presence of vibrations the unloading curves still follow a JKR-like curve (Johnson et al., 1971) but with an increased effective work of adhesion. Upon dynamic actuation, the contact area quickly transitioned from the "static" to the "dynamic" JKR (Johnson et al., 1971) curve, yielding a maximum 14-fold enhancement of the pull-off force with respect to F^0_{PO}. Both studies (Shui et al., 2020) (Tricarico et al., 2025) reported saturation of adhesion enhancement beyond a threshold amplitude, after which abrupt degradation of the adhesive properties is observed. Tricarico et al. (2025) introduced a lumped dynamic model for vibroadhesion based on a static characterization of the adhesive properties of the interface through the Gent- Schultz law, which was obtained fitting the results of several unloading tests conducted *without* dynamic excitation. The determined Gent- Schultz law was then included in the dynamic lumped model, which provided very good predictions of the interfacial stickiness in vibroadhesion experiments.

A recent work by Yi et al. (2024) has focused more on the possibility to include vibroadhesion into a soft end-effector for robotic applications. Differently from Refs. (Shui et al., 2020) (Tricarico et al., 2025), Yi et al. (2024) have considered a vibrating PDMS hemisphere in contact with a silicon wafer, demonstrating that the vibroadhesion-based modulation can be effectively exploited to increase or weaken adhesion, where controllable weakening typically happening at low vibration amplitude ($\sim 5\ \mu$ m). They studied the effects of sphere radii (ranging from 1 to 5 mm) surface roughness and material properties (via different PDMS formulations). For a 1 mm radius, they reported a 25-fold enhancement and a 50% reduction in pull-off force, relative to their static indentation tests. Their results showed that maximum pull-off force scaled linearly with sphere radius, in agreement with JKR theory, suggesting size-independent enhancement of the effective work of adhesion. Surface roughness was found to consistently reduce adhesion enhancement already with roughness peak-to-valley $R_Z \approx 10\ \mu$ m.

Chen et al. (2025) exploited the idea of using vibration to modulate not only normal but also tangential forces. They developed a vibration-programmable adhesion/friction system consisting of a bio-inspired pad with graded mechanical properties (obtained via graded magnetic particle distribution). Their design achieves exceptionally high shear strength (> 130 kPa), fast response times (< 30 ms), and robust performance across tilted, rough, and vibrated surfaces.

From the theoretical perspective a few efforts have been made to model the vibroadhesion phenomenon, mostly based on simplified lumped models, both neglecting (Argatov et al., 2025; Ciavarella et al., 2025) and including (Shui et al., 2020; Tricarico et al., 2025) dynamic effects, with the latter models considering the indenter as a nonlinear oscillator. Thus far, they are all based on the traditional JKR theory (Johnson et al., 1971) extended to account for viscoelasticity through a phenomenological Gent-Schultz law.

The aim of this work is to explore how design parameters such as substrate thickness t, radius of the indenter R, material properties, unloading rate r and preload F_{cO} affect the adhesive performance of vibration-assisted interfaces, in particular the pull-off force F_{PO}, the contact radius a, the mean stress at pull-off σ_{PO}, the maximum adhesion enhancement F_{PO}/F^0_{PO} and the range of vibration amplitudes that sustain adhesion enhancement. Our results offer insights into the influence of individual design choices on vibroadhesion performance, including the design of grippers, manipulators, and adhesive pads. We found that $\{F_{PO}, \sigma_{PO}, F_{PO}/F^0_{PO}\}$ are highly influenced by the substrate thickness, the radius of the sphere and the PDMS crosslink ratio (which in turns modify both the relaxed Young modulus E_0 and $\Delta\gamma_0$), while the imposed unloading rate r and the preload F_{cO} are minimally influent. Interestingly we find that the maximum average stress at pull-off ($\sigma_{PO} = 186$ kPa) was obtained with the spherical indenter having the smallest radius of curvature ($R = 13.1$ mm), indicating the viability of vibroadhesion also for miniaturized grippers and manipulators. Finally, we show that a simplified numerical model for vibroadhesion, developed in Ref. (Tricarico et al., 2025), can predict the same trends we had observed experimentally. Ultimately, this work establishes the relative importance of geometrical and rheological factors in determining the performance of vibration-modulated adhesive interfaces and provides design guidelines for devices exploiting vibroadhesion in applications requiring tunable or selective adhesion.

2. Methods

2.1. PDMS synthesis

The PDMS substrates were made using the commercial silicone Dow Sylgard 184®. Three batches were prepared, each with a different base-to-curing agent weight ratio (5:1, 10:1, 20:1). The base and curing agents were thoroughly mixed by magnetic stirring for 30 min and then degassed under vacuum for 20 min at room temperature. The resulting resin was then cast into petri dishes containing a glass slide (2.5 × 2.5 cm in-plane dimensions) previously treated with air plasma to enhance bonding. For the PDMS 10:1 four sub-batches were prepared, in order to get samples with different thicknesses ($t = 1, 3, 5,$ and 10 mm). For all the samples, curing was carried out in two stages: 48 h at room temperature followed by 90 min at 75 °C. This curing procedure, adapted from Delplanque et al. (2022), minimizes shrinkage-related warping, preserving a flat surface.

2.2. Vibroadhesion tests

The experimental apparatus (shown in Fig. 1a and schematized in Fig. 1b) has been thoroughly described in Ref. (Tricarico et al., 2025). The PDMS samples were fixed onto a PMMA transparent beam, mounted on two electrodynamic shakers (Dynalabs DYN-PM-250), that provided the actuation. The PDMS sample was centered between the shakers, and

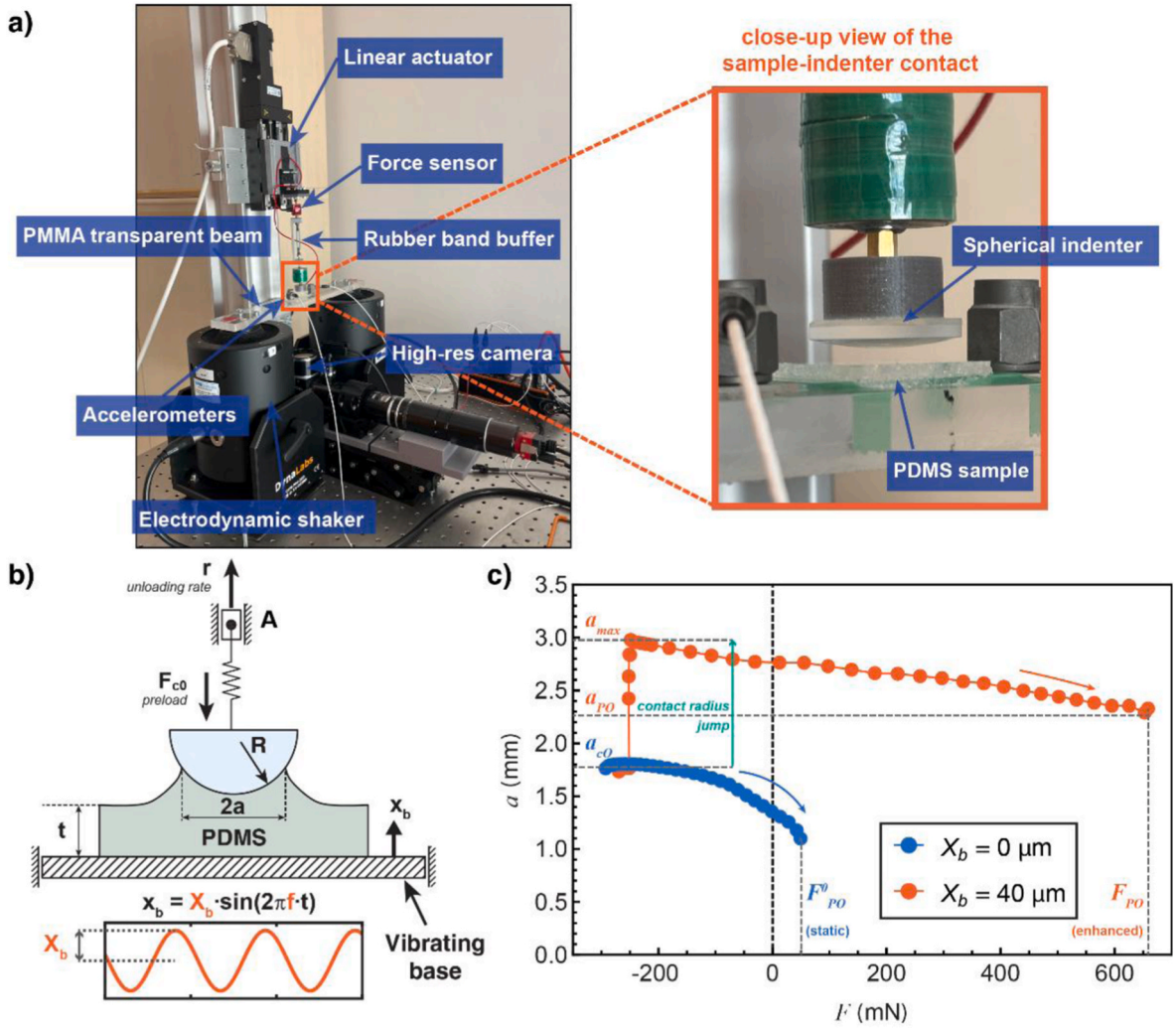

Fig. 1. *a) Vibroadhesion test setup, picture. b) Schematic of the vibroadhesion test setup. The motion of point "A" is controlled in order to get the desired loading/unloading protocol. c) Example of a typical contact radius versus force curve during unloading in a vibroadhesion test (orange curve, $X_b = 40$ μm, $f = 300$ Hz) and in a static test (blue curve, $X_b = 0$). The data correspond to PDMS 10:1, $t = 3$ mm, $R = 51.5$ mm, $r = 5$ μm/s, $F_{c0} = -250$ mN). The main features such as contact area jump and pull-off instability points are highlighted. (For interpretation of the references to colour in this figure legend, the reader is referred to the Web version of this article.)*

two piezoelectric accelerometers (DYTRAN 3055D1, 1–10,000 Hz) positioned symmetrically beside it recorded the beam acceleration. The input vibration amplitude X_b was obtained via real-time double integration of the acceleration signals. Data was acquired using a Dewesoft KRYPTON-6XSTG data acquisition system.

Three borosilicate glass lenses were employed as indenters (radii of curvature $R = 13.1, 25.6$ and 51.5 mm). Vertical approach and detachment of the spherical indenters from the PDMS sample were performed by motorized micrometric linear stage (Physik Instrumente, M-403.2DG). The contact forces were measured by a force sensor (a uniaxial S-beam load cell Futek LSB205, natural frequency 1180 Hz, resolution 1 mN) placed between the sphere and the linear stage. To isolate the load cell from high-frequency axial vibrations, a pre-tensioned rubber band was inserted as a compliant buffer between the indenter and the load cell. A calibration of the rubber element was performed by recording force–displacement curves at the same loading rate used in testing, yielding an estimated stiffness of $k = 320$ N/m.

Contact area imaging was performed using a high-resolution camera (Alvium, 1800 U-2040 m, 20 MP, pixel size 2.74 μm, max frame rate 10 fps, shutter exposure time 5ms), placed beneath the sample. The contact radius was determined from optical images of the contact area by post-processing the acquired frames using a custom image analysis routine, implemented in *Wolfram Mathematica*.

The testing protocol consists of a loading phase, up to a set preload of $F_{c0} = -250\,mN$, with a loading rate of 100 μm/s, followed by a 60 s dwell period to allow for material relaxation. Then, the substrate vibrations were activated manually by adjusting the amplifiers gain. Following an additional 60 *s* stabilization phase, the sample was unloaded at an unloading rate of $r = 5$ μm/s. All experiments were conducted at a room temperature of approximately 20 °C.

Each test was performed three times: during every trial the force–time signal was recorded, while images of the contact area were captured only once.

2.3. Characterization of interfacial adhesion

To characterize the rate-dependent adhesive behavior of the PDMS–glass interfaces, we first measured their quasi-static properties ($E_0^*, \Delta\gamma_0$) using a classical JKR indentation test. The indenter was driven into the PDMS substrate at a loading rate of 100 μm/s, after which the contact was held for 60 s to allow material relaxation. The unloading phase was then performed at $r = 1$ μm/s. Note that the unloading rate used in this section ($r = 1\ \mu$m/s) refers only to the quasi-static characterization tests (JKR fitting), whereas a higher unloading rate ($r = 5\ \mu$m/s) was employed in vibroadhesion experiments, as described in Section 2.2.

The resulting unloading curve, representing the relationship between contact radius and contact force, was fitted using the JKR model (Eq. (2)) to extract the work of adhesion ($\Delta\gamma_0$) and the relaxed contact modulus (E_0^*).

$$F = -\frac{4E^* a^3}{3R} + \sqrt{8\pi\Delta\gamma_0 E_0^* a^3} \tag{2}$$

A summary of the material properties obtained for the PDMS 5:1, 10:1 and 20:1 is reported in Table 1, while the full experimental data with the relative JKR fits are shown in Fig. S1. As expected, we found that PDMS layer with high base-cure agent ratio are more compliant and stickier. We found that the PDMS 5:1 layer was 3.6 times stiffer than the PDMS 20:1 layer, while as regards $\Delta\gamma_0$ the PDMS 20:1 layer was about 2.7 times stickier than the PDMS 5:1 layer. For the rate-dependent interfacial characterization, the layer with thickness $t = 5$ mm was used. We conducted adhesion tests where the indenter was unloaded from a relaxed substrate, after a long dwell time, at different unloading rates ranging from 1 to 1000 μm/s. By post-processing the experimental results obtained and using the JKR contact model the effective work of adhesion $\Delta\gamma_{eff}$ can be obtained

$$\Delta\gamma_{eff} = \frac{(F_H - F_C)^2}{6\pi R F_H} \tag{3}$$

where $F_H = \left(4\,E_0^*\,a^3\right)/(3R)$ is the Hertzian load, a is the contact radius, R is the sphere radius, and F_C is the normal contact force measured by the load cell. The empirical Gent-Shultz model (Eq. (1)) was used to determine the parameters v_0 and α for each sample (see Table 1). The resulting Gent-Shultz curves are shown in Fig. S2 and Fig. S3. We found α in the range $0.55 - 0.65$ while as regards v_0, it diminishes while increasing the base to cure agent ratio, implying in softer layers viscoelastic dissipation is activated at a lower crack velocity.

3. Experimental results

Fig. 1 shows an example of a typical indentation test for a PDMS 10:1 layer with thickness 3 mm and using the indenter with radius of curvature $R = 51.5$ mm: the evolution of the contact radius a versus the contact force F is shown for a classical static (i.e. with $X_b = 0$, blue curve) and dynamic (i.e. with $X_b > 0$, orange curve) test. We will define "static" and "dynamic", the tests for which $X_b = 0$ or $X_b > 0$ respectively, during the unloading phase. In both tests the interface was preloaded at $F_{c0} = -250$ mN and let to relax after loading without vibrations. In the static test once the unloading phase starts at $r = 5\,\mu m/s$ the contact radius shrinks continuously, up to the instability point, where, in this test, the maximum adhesive force (pull-off) measured was $F_{PO} \cong 49$ mN. In the dynamic test, after substrate relaxation, vibrations are activated ($X_b = 40$ μm; $f = 300$ Hz) resulting in a sudden jump of the contact radius from $a_{c0} \cong 1.8$ mm to $a_{max} \cong 2.9$ mm, which represents an increase of about 61%. Note that the presence of the compliant rubber band from which the indenter is suspended does not result in a change in the preload, which remains close to 250 mN. In the dynamic test the unloading phase starts at a contact radius markedly larger than the static test and detachment takes place at an instability point, where the pull-off force is about 660 mN, i.e., 13 times larger than the static value in the same conditions.

In the following we will refer to a_{max} as the maximum contact radius reached once vibrations are activated, a_{c0} the contact radius under the preload F_{c0} without vibrations, a_{PO} the contact radius at pull-off (Fig. 1c). In the remainder of this manuscript, the effects of sample thickness, sphere radius, PDMS crosslinking ratio, unloading rate, and preload are investigated.

Table 1
Material properties and Gent-Schultz parameters of the PDMS samples.

Sample		Static material properties		Gent-Shultz parameters	
material	Thickness (mm)	E_0^* (MPa)	$\Delta\gamma_0$ (mJ/m^2)	v_0 (mm/s)	α
PDMS 5:1	5	5.4	143	0.0963	0.614
PDMS 10:1	5	2.7	202	0.0786	0.654
PDMS 20:1	5	1.5	380	0.0284	0.558

3.1. Effect of sample thickness

Vibroadhesion tests were carried out on the four PDMS 10:1 samples, with thickness $t = [1,3,5,10]$ mm and using the indenter with radius of curvature $R = 51.5$ mm. The actuation frequency was set to $f = 300$ Hz, while the amplitude X_b were set to 0 (i.e., no vibrations), 20, 40, 60 and 80 μm. During unloading the free end of the spring (point A in Fig. 1b) was driven at the rate of $r = 5$ μm/s, which for the static test without vibrations resulted in a pull-off force of $F_{PO} \sim 58$ mN for all the thicknesses considered.

As illustrated in Fig. 2a, the substrate thickness strongly affects the range of amplitudes over which enhancement is observed. This range widens as the thickness increases from 1 to 5 mm and then narrows again with $t = 10$ mm. Interestingly, the maximum amplification of the pull-off remains nearly constant with thickness ($\sim 11 - 13$ times the static value), but it can be reached at lower amplitudes for the thinnest layer. For instance, a maximum pull-off force of $F_{PO} = 735$ mN can be reached at $X_b = 20$ μm for $t = 1$ mm, while a maximum $F_{PO} = 799$ mN is recorded at $X_b = 60$ μm for $t = 5$ mm.

Once the vibrations are activated, the maximum contact radius a_{max} increases monotonically with X_b (Fig. 2b), which we relate to larger oscillations of the contact radius during one vibration period, that leads to an increased viscoelastic dissipation at the crack tip resulting in a greater apparent surface energy (Shui et al., 2020; Tricarico et al., 2025; Argatov et al., 2025; Ciavarella et al., 2025). Comparing Fig. 2a and b, it can be observed that even when the pull-off force starts declining the maximum contact radius does not. This results in a reduction of the mean stress at pull-off $\sigma_{PO} = F_{PO}/\left(\pi a_{PO}^2\right)$, which can be seen in Fig. 2c. Generally, we found σ_{PO} decreases with X_b in all cases, except for $t = 5$ mm when it peaks at $X_b = 20$ μm (Fig. 2c). Fig. S8 reports the measured contact radius at pull-off a_{PO} for all the tests shown in Fig. 2.

Inspection of micrographs of the contact area patch at pull-off as a function of the base vibration amplitude X_b and for all the thicknesses (Fig. S4) provides insights in the mechanism leading to the unstable detachment of the interface. Fig. 2d reports the case related to the thickness $t = 10$ mm. As the vibration amplitude increases, radial surface instabilities (wrinkles) appear at the contact periphery (see also Ref (Tricarico et al., 2025).). In all the tests the pull-off force strongly reduced when wrinkles appeared on a large region of the contact area as it can be noticed for the $t = 1$ mm sample at $X_b = 40$ μm (Fig. S4) and for $t = 10$ mm at $X_b = 60$ μm (Fig. 2d).

The substrate thickness t strongly influences how the base vibration is transmitted to the PDMS-indenter interface. The thicker the sample the further the excitation is applied with respect to the contact interface. Moreover, from the quasi-static JKR fit of the contact radius versus normal force curves, it appeared that the effective modulus obtained from the JKR model decreases for thicker layers (see Table S1), as the PDMS slab is bonded to a glass slide which may be considered rigid with respect to the PDMS. Hence, for a given vibration amplitude, thinner layers transmit stronger excitation to the contact interface, which explains why at low vibration amplitudes thinner layers exhibit larger enhancement of the pull-off force. This phenomenon may be exploited to efficiently design adhesive pads that require smaller actuation amplitudes to obtain similar adhesive performance. At large vibration amplitudes nonlinear phenomena resulting in interfacial instabilities (wrinkles) have been observed for all the thickness tested, suggesting that this is the main mechanism degrading the adhesive performance of

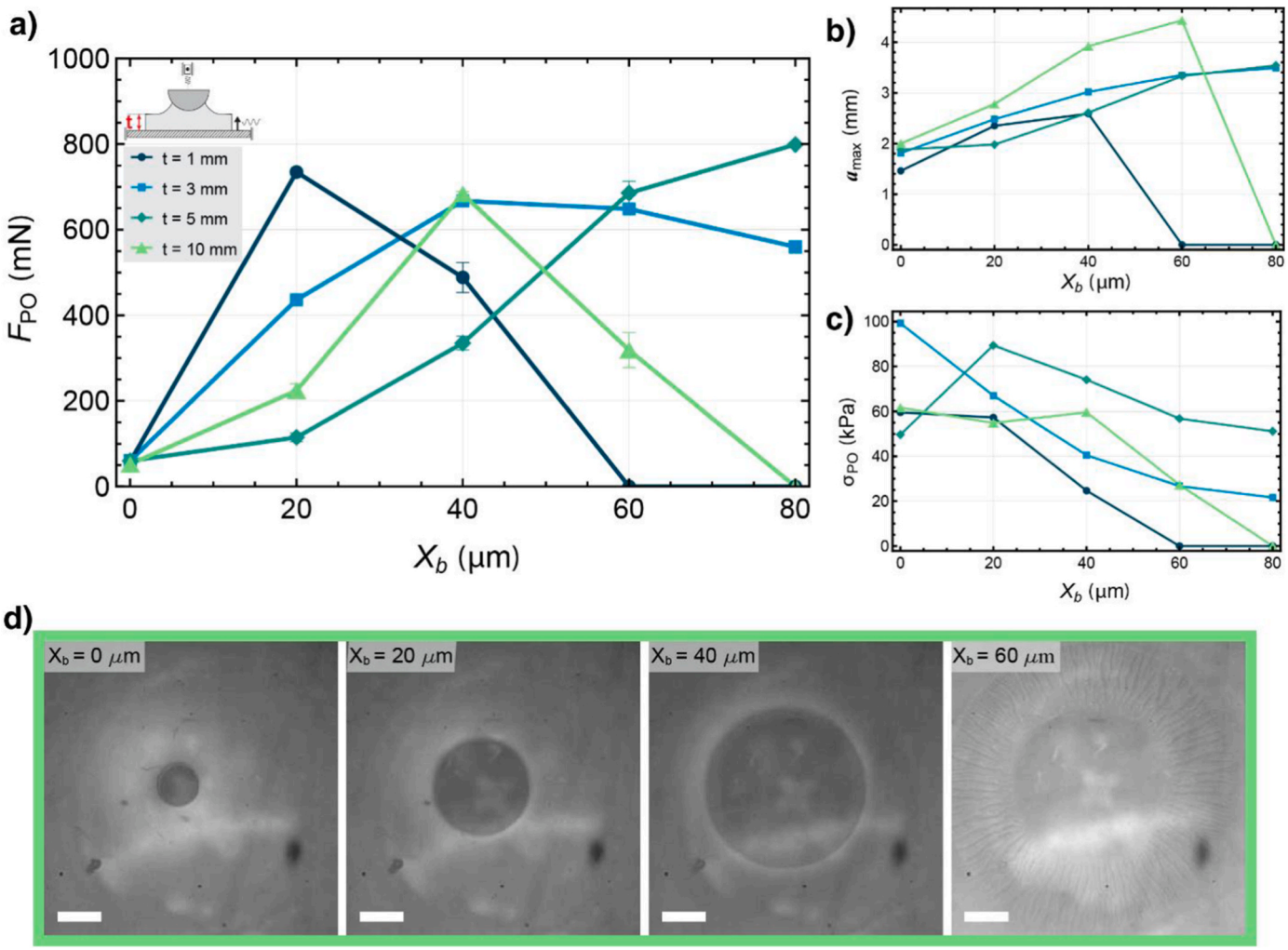

Fig. 2. Effect of thickness. Evolution of a) pull-off force, b) max contact area and c) pull-off stress with varying vibration amplitude of the base. d) Micrographs of contact area at pull-off for each X_b for the sample $t = 10$ mm (scale bars 1 mm). The tested material was PDMS 10:1, the other parameters were fixed to: $R = 51.5$ mm, $r = 5$ μm/s, $F_{c0} = -250$ mN. Error bars indicate the standard deviation calculated from three test repetitions.

vibroadhesive interfaces.

3.2. Effect of sphere radius

To examine the influence of the indenter radius of curvature, three borosilicate glass lenses with radii $R = [13.1, 25.6, 51.5]$ mm were tested on a PDMS 10:1 layer of thickness $t = 5$ mm at $f = 300$ Hz and $X_b = [0, 20, 40, 60, 80]$ μm. Fig. 3a shows the pull-off force evolution with X_b for each indenter employed. In the static tests the pull-off forces scaled with radius as one would expect from JKR theory, nevertheless in the dynamic tests the same scaling is not preserved, with the indenter with radius $R = 25.6$ mm showing better adhesive performance at $X_b = 40$ μm with respect to both the indenters with smaller and larger radius of curvature, but then showing very low adhesion for $X_b \geq 60$ μm. The radius of curvature affects also the width of the amplitude range over which adhesion enhancement takes place, although we could not identify a clear trend. Fig. 3b shows the pull-off enhancement which is the pull-off force (F_{PO}) normalized by its static value obtained for each indenter (F^0_{PO}). Fig. 3b indicates that, when normalized, the maximum enhancement obtained is similar for all the indenters (in the range $\sim 11 - 14$) irrespectively of their radius of curvature. Also, at low vibration amplitude, the smaller radii of curvature provide a greater enhancement, while the indenter with $R = 51.5$ mm still sustains a large adhesive force for strong base excitation $(F_{PO}/F^0_{PO} \cong 14$ at $X_b = 80$ μm$)$. Interestingly, before surface instabilities appeared, we found the mean stress at pull-off σ_{PO} for the indenter with the smallest radius of curvature ($R = 13.1$ mm) to be in the range of $\sigma_{PO} = 150 - 200$ kPa, outperforming the larger radii indenters ($R = 25.6$ mm and $R = 51.5$ mm) for which $\sigma_{PO} = 50 - 100$ kPa, a typical range in our experiments (Fig. 3c). This result suggests that miniaturization of vibroadhesive pad design might be possible, without degradation of their adhesive performance.

The maximum contact area reached during the tests increases with X_b, consistently to what was observed for varying thickness (Fig. S6). Micrographs of the contact area patch at pull-off for all the indentation tests are shown in the SI (Fig. S5) while Fig. 3d the micrographs relative to the indenter with radius $R = 25.6$ mm are shown. Inspection confirms also in this case that the pull-off force abruptly reduces when surface instabilities appear surrounding the contact patch, as observed in Fig. 2d.

3.3. Effect of PDMS mixing ratio

In order to explore the effect of different material properties on the vibroadhesive performance, we carried out the same set of vibroadhesion test ($f = 300$ Hz, $X_b = [0, 20, 40, 60, 80]$ μm) on PDMS substrates with thickness $t = 5$ mm prepared with different mixing weight ratios (i.e., base: crosslinker), namely 5:1, 10:1 and 20:1. The mixing ratio reg-

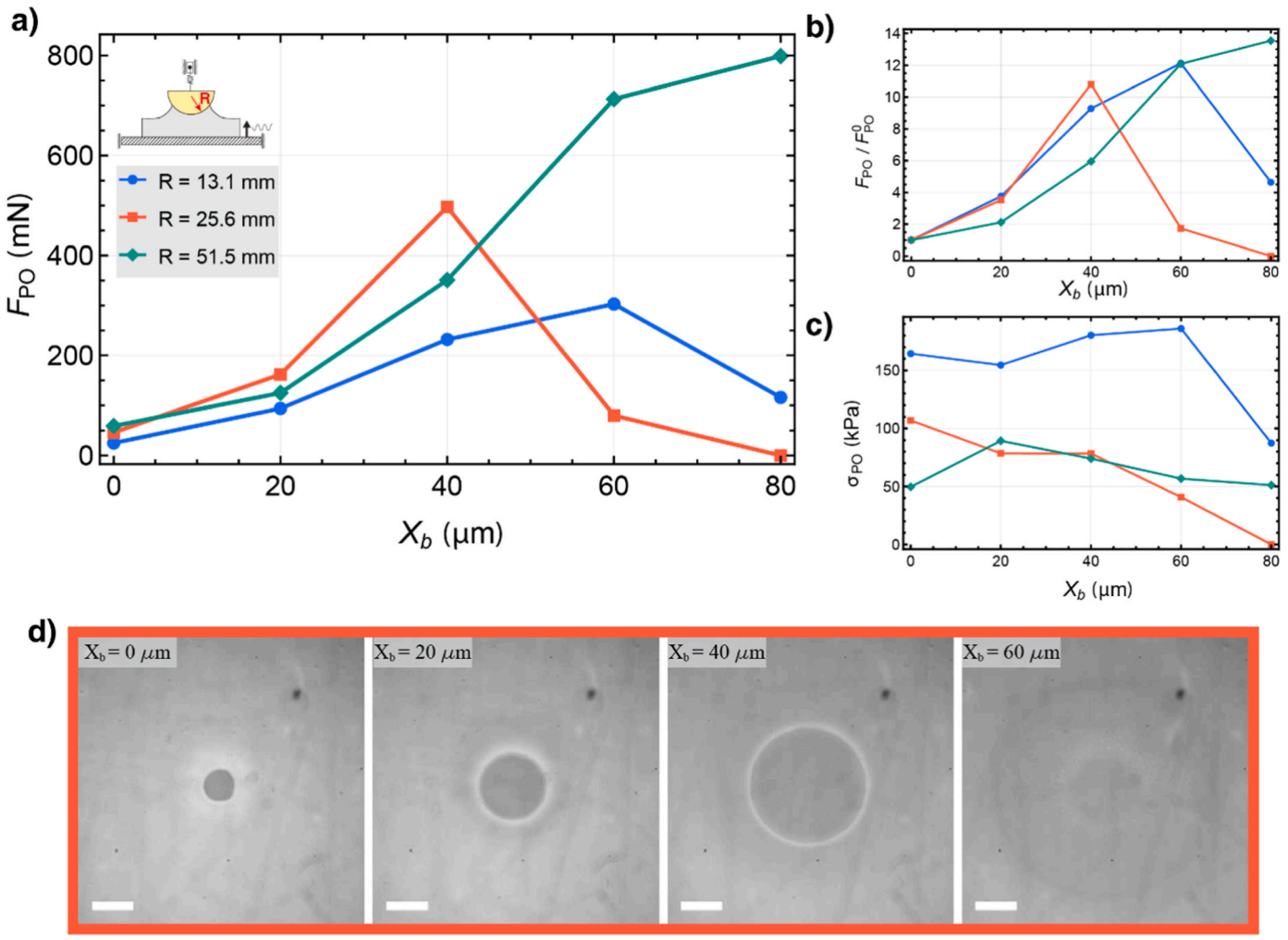

Fig. 3. *Effect of sphere radius. Evolution of a) pull-off force, b) pull-off normalized by its static value and c) pull-off stress with varying amplitude of the base vibrations for* $R = [13.1, 25.6, 51.5]$ mm. *d) Micrographs of contact area at pull-off for each* X_b*, for the sphere* $R = 25.6$ *mm (scale bars* 1 mm*). The tested material was PDMS 10:1, the other parameters were fixed to:* $t = 5$ *mm,* $r = 5$ *μm/s,* $F_{c0} = -250$ *mN.*

ulates the crosslink density, affecting both the elastic modulus and the work of adhesion (see Table 1). In particular, the composite elastic modulus decreases and the work of adhesion increases with crosslink density.

As shown in Fig. 4a, the material composition significantly affects the amplitude window for enhancement. As seen in Fig. 3a the PDMS 10:1 substrate exhibits a monotonous enhancement with amplitude within the 0 − 80 μm range, contrary to its 20:1 and 5:1 counterparts. In PDMS 20:1, pull-off force peaks at 60 μm and then decreases, while in PDMS 5:1 it peaks already at 20 μm and then suddenly drops to 0 at 40 μm. This behavior strongly resembles that observed in Fig. 2 changing the thickness of the substrate: stiffer materials or thinner substrates improve adhesion enhancement at low vibration amplitudes, nevertheless Fig. 4a shows that in absolute value the softer and stickier material (PDMS 20:1) can reach very high adhesive forces ($\max(F_{PO}) \cong 1300$ mN) compared to the low crosslink ratio PDMS substrates. The behavior of PDMS 5:1 resembles the one of PDMS 10:1 with $t = 1$ mm (Fig. 2), with a large enhancement already occurring at low $X_b = 20$ μm, followed by adhesion suppression for larger oscillations.

When we analyze the maximum contact area (Fig. 4b) and the contact area at pull-off (Fig. S8c) we observe trends similar to Fig. 2b and Fig. S8a, respectively, with a_{MAX} increasing with X_b across the whole range, while a_{PO} decreases when the pull-off force decreases. In terms of pull-off stress (Fig. 4c), σ_{PO} remains in the usual range of 50− 100 kPa, generally decreasing with the vibration amplitude X_b. Consistently with previous results, we find in PDMS 20:1 that the reduction of pull-off force between $X_b = 60$ μm and 80 μm coincides with the onset of radial wrinkling at the contact edge (Fig. 4d and Fig. S5).

3.4. Effect of unloading rate

The influence of unloading rate was investigated using the PDMS 20:1 substrate, with thickness $t = 5$ mm and radius of the indenter $R = 51.5$ mm. Vibroadhesion tests were performed with the standard loading protocol ($F_{c0} = -250$ mN), this time employing unloading rates covering two orders of magnitude (5, 50 and 500 μm/s). We observed that, when $X_b > 0$, the unloading rate has a small effect on the pull-off forces, even negligible up to 50 μm/s. This is in contrast with the static case (i.e., $X_b = 0$) where changing the unloading rate from 5 to 500 μm/s is sufficient to enhance the pull-off force from $F_{PO} = 136$ mN to $F_{PO} = 382$ mN, a factor ∼ 3. (Fig. 5a). If we observe the pull-off enhancement F_{PO}/F^0_{PO}, considering as a reference the pull-off force F^0_{PO} obtained under static conditions for each value of r (Fig. 5b), it is clear how the effect of microvibrations becomes less significant with increasing r. In other words, the larger the rate of unloading the smaller the toughening effect that can be obtained by superposing high frequency microvibrations. The maximum enhancement (with respect to the non-vibrating case) always occurred at $X_b = 60$ μm, but dropped from ∼10 to ∼4 by increasing the unloading rate from 5 to 500 μm/s. Notice that at high unloading rates the application of microvibrations can result in a slight

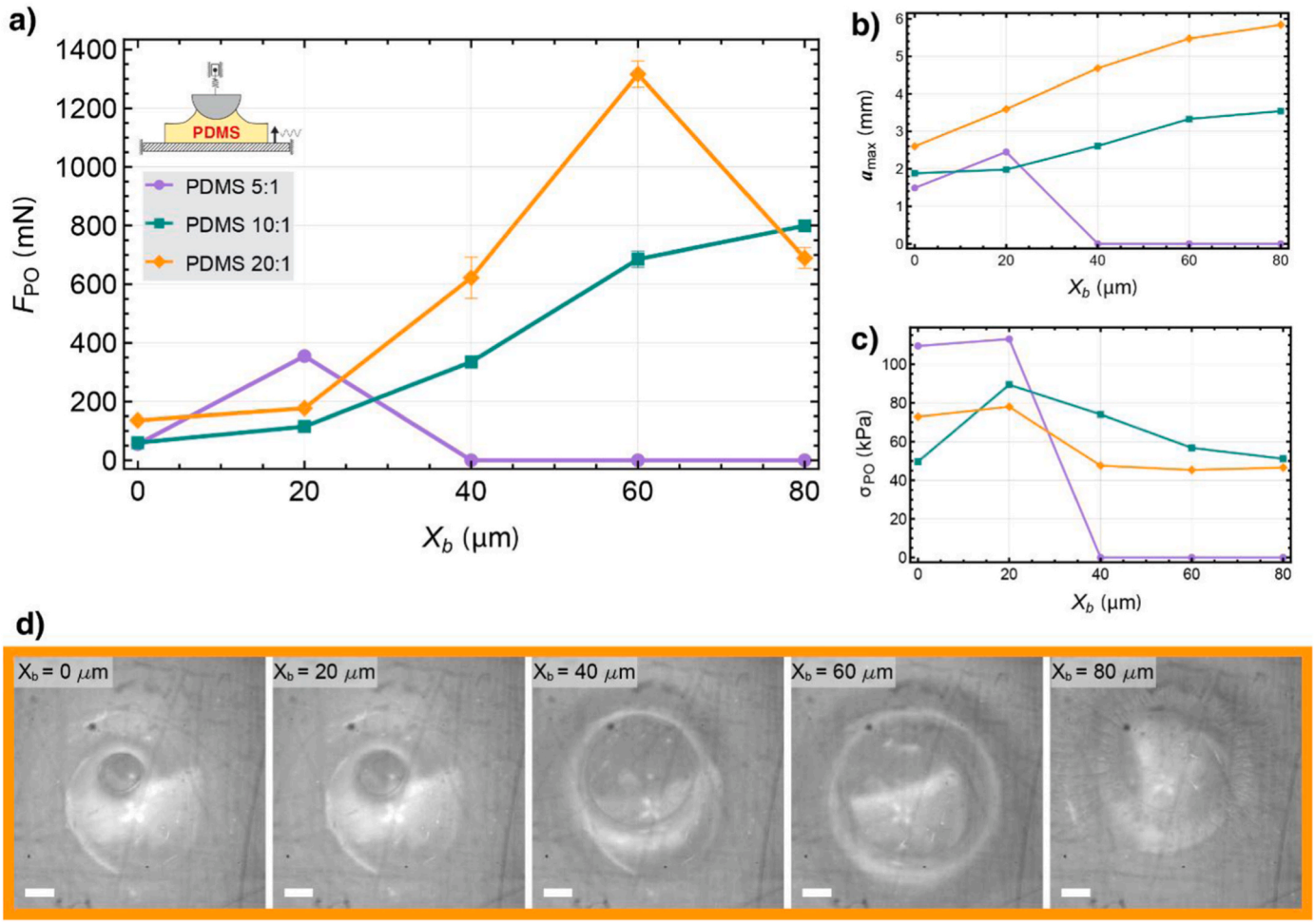

Fig. 4. Effect of PDMS mixing ratio. Evolution of a) pull-off force, b) max contact area (at dwell time) and c) contact area at pull-off with varying amplitude of the base vibrations. d) Micrographs of contact area at PO for each X_b for the sample PDMS 20:1 (scale bars 1 mm). The other parameters were fixed to: $t = 5$ mm, $R = 51.5$ mm, $r = 5$ μm/s, $F_{c0} = -250$ mN. Error bars indicate the standard deviation calculated from three test repetitions.

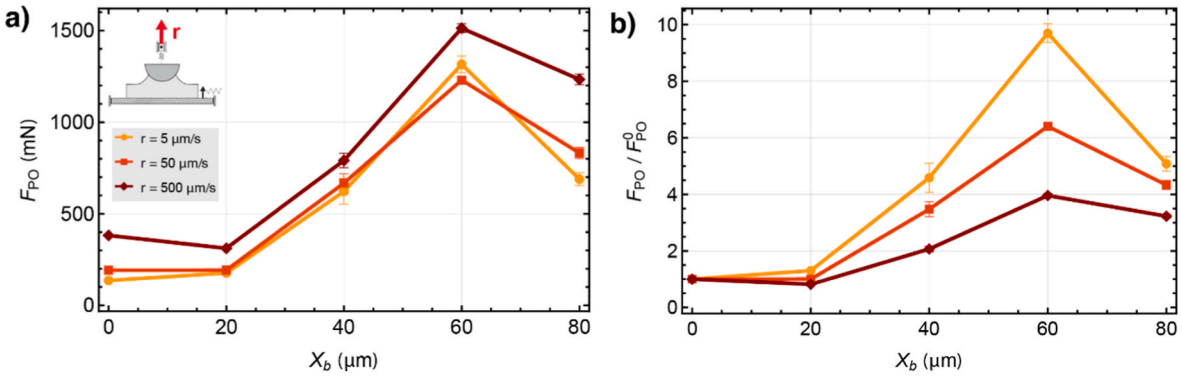

Fig. 5. Effect of unloading rate. Evolution of a) pull-off force, b) pull-off enhancement (with respect to the case $X_b = 0$ at each r) with varying amplitude of the base vibrations. c) Evolution of pull-of enhancement with r, with varying X_b. The tested material was PDMS 20:1, the other parameters were fixed to: t = 5 mm, R = 51.5 mm, $F_{c0} = -250$ mN. Error bars indicate the standard deviation calculated from three test repetitions.

decrease in the pull-off force (see Fig. 5, $X_b = 20$ μm; $r = 500$ μm/ s and Fig. S10). Analogously to pull-off force, also a_{max}, σ_{PO} and a_{PO} (Fig. S8 and S10, respectively) are only slightly affected by the unloading rate variation.

3.5. Effect of preload

Finally, we studied the effect of preload on the pull-off enhancement. We performed vibroadhesion tests on a PDMS 20:1 substrate, 5 mm thick, fixing $r = 500$ μm/s and $R = 51.5$ mm. Every indentation test was repeated with three different preloads of $F_{c0} = -400$ mN, $F_{c0} = -250$ mN and with vanishing preload $F_{c0} \cong 0$ mN (prior to base excitation,

the indenter was slowly approached to the substrate surface, just until the "jump into contact" occurs). The results of the three series of tests are compared in Fig. 6.

Fig. 6a shows the pull-off force as a function of the base vibration amplitude X_b for the three preloads studied. By comparing the pull-off force results from the three sets of experiments it is clear that while the preload strongly affects the pull-off force in static experiments ($X_b = 0$) it has almost no influence in vibroadhesion tests (Fig. 6a). As shown in Fig. 6b, for $X_b > 20$ μm, once actuation begins, the contact radius rapidly transitions to its "amplified" value, regardless of the initial preload. For $X_b = 20$ μm, increasing the preload leads to an approximately 25% increase in the contact radius; however, this change is insufficient to produce a corresponding rise in pull-off force. Similarly, the pull-off stress (Fig. 6c) and the contact radius at pull-off (Fig. S8e) remain largely unaffected by the preload.

4. Numerical predictions

We employed the numerical model developed in Ref (Tricarico et al., 2025). to qualitatively predict the trends observed in the experimental campaign. We adopted the "high-frequency model", which simplifies the adhesive contact problem by neglecting the dynamics of the nonlinear mass-spring system. The contact interactions are described via the JKR contact model (Johnson et al., 1971) enhanced with an effective surface energy accounting for the viscoelastic dissipation at the crack tip. Inverting the Gent-Schultz (Gent and Schultz, 1972) law (Eq. (1)), with the hypothesis to neglect the oscillator dynamical response one obtains (Tricarico et al., 2025)

$$\dot{a}(t) = \begin{cases} -v_0 \left[\dfrac{E^*}{2\pi\, a \Delta\gamma_0} \left(\dfrac{a^2}{R} - \delta \right)^2 - 1 \right]^{\frac{1}{\alpha}}, \dot{a}(t) < 0, \\ v_0 \left[\dfrac{2\pi\, a \Delta\gamma_0}{E^*} \left(\dfrac{a^2}{R} - \delta \right)^{-2} - 1 \right]^{\frac{1}{\alpha}}, \dot{a}(t) > 0, \end{cases} \tag{4}$$

where a dot superposed indicates a time derivative hence the crack speed is $v = -\dot{a}$. The indentation depth $\delta(t) = \delta_0 + r_\delta t + X_b \sin(2\pi f\, t)$ is imposed by the loading protocol, with r_δ being the rate of unloading of the rigid sphere and δ_{c0} the indentation under the preload F_{c0}, according to the JKR model (Johnson et al., 1971) with relaxed elastic modulus.

Integrating the ODE in Eq. (4) yields the time evolution of the contact radius $a(t)$ and the corresponding force history $F(t)$ follows directly from the JKR model (see Ref. (Tricarico et al., 2025) for the detailed derivation). The model assumes a rigid sphere indenting an elastic half-space and therefore does not capture finite-thickness effects. Variations in sample material and thickness were simulated solely through changes in the effective modulus E^*, while parameters such as sphere radius, unloading rate, and preload were varied directly. The input parameters employed in the simulations are listed in Table S2 and are typical for a soft silicone.

The numerical results are shown in Fig. 7. Increasing the sample elastic modulus (Fig. 7a) leads to a large pull-off force enhancement at smaller X_b, consistent with our experimental observations for decreasing thickness (Fig. 2a) and stiffer PDMS formulations (Fig. 4a). It should be emphasized that the model is based on linear elasticity and therefore does not incorporate nonlinear phenomena, such as wrinkle formation (Tricarico et al., 2025), that are responsible for the decay of the pull-off force at large vibration amplitudes. The simulations also predicted an inverse proportionality of pull-off force enhancement with the sphere radius (Fig. 7b). Experimentally (Fig. 3b), this trend is observed only at small amplitudes (i.e., $X_b = 20$ μm); at larger amplitudes, nonlinear interfacial instabilities appear earlier for smaller spheres, as confirmed by micrographs of the contact patch near pull-off (Fig. S5), which makes this trend difficult to observe on large range of substrate vibration amplitudes. The unloading rate was found to affect the pull-off force only for small vibration amplitudes X_b (Fig. 7c), in good agreement with the experimental trend (Fig. 5a). Notice that, in the numerical simulation the sphere is unloaded at a prescribed rate r_δ, whereas in the experiments the controlled parameter is the retraction velocity of the slider r (point A in Fig. 1a), which is larger than the actual unloading rate experienced by the indenter, due to the presence of the rubber band buffer. Finally, the numerical model reproduced the negligible influence of the preload on pull-off force (Fig. 7d), in agreement with the experimental findings (Fig. 6a).

5. Discussion

We have presented a comprehensive experimental investigation exploring the effect of material and geometrical parameters including substrate thickness t, indenter radius R, material properties (E_0^*, $\Delta\gamma_0$),

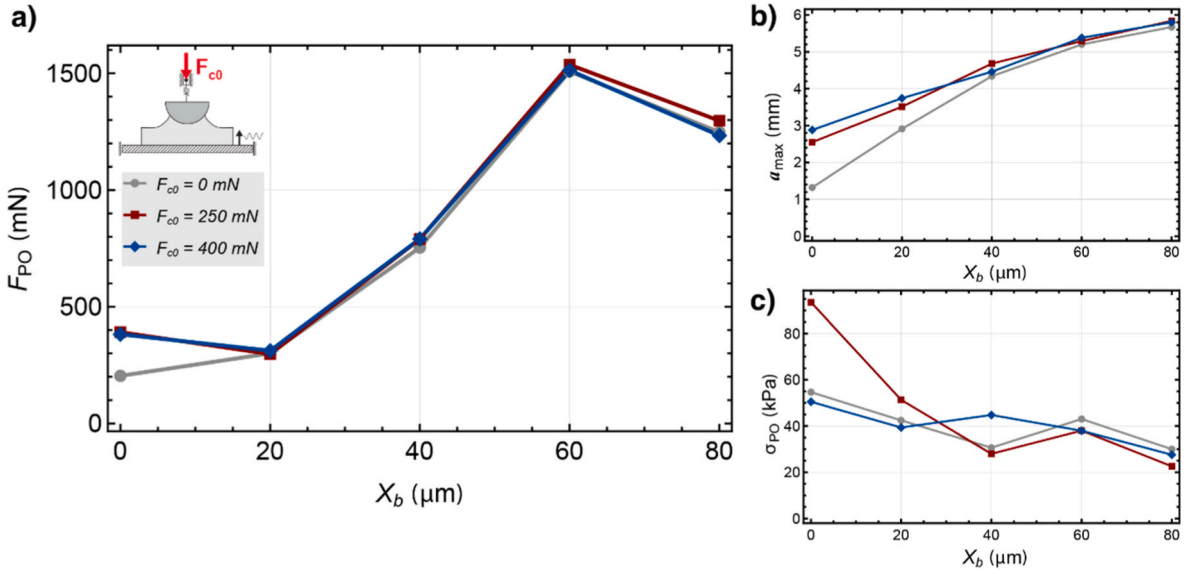

Fig. 6. Effect of preload. Evolution of a) pull-off force, b) max contact area and c) pull-off stress with varying vibration amplitude of the base. The tested material was PDMS 20:1, the other parameters were fixed to: $t = 5$ mm, $R = 51.5$ mm, $r = 500$ μm/s. Error bars indicate the standard deviation calculated from three test repetitions.

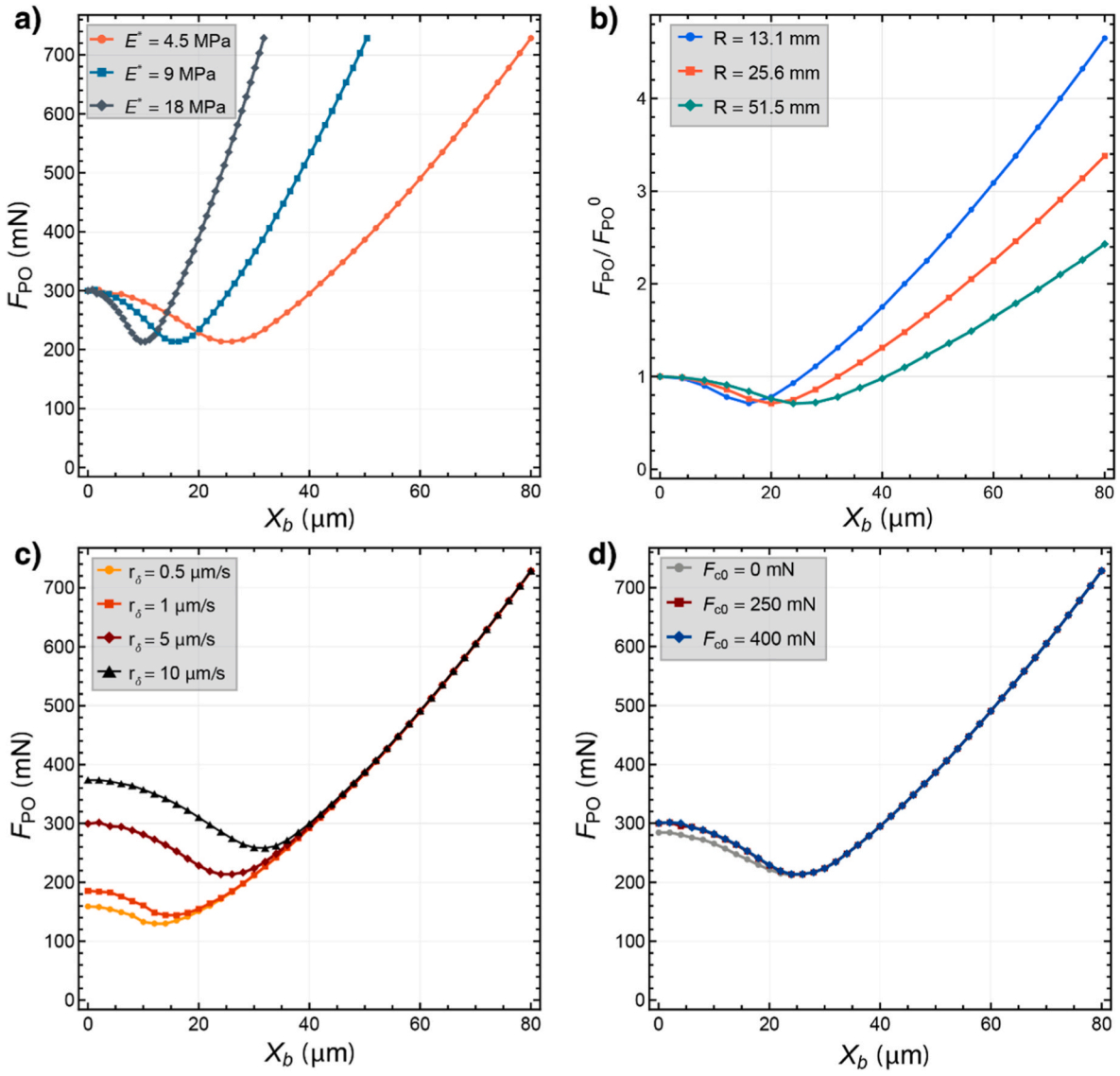

Fig. 7. Numerical results illustrating the dependence of pull-off force on vibration amplitude for different (a) effective contact modulus, (b) sphere radius (reported as pull-off enhancement with respect to the static test), (c) unloading rate, and (d) preload.

unloading rate r, and preload F_{c0}, on the adhesive performance of vibration-modulated soft contacts. In particular we focused on the pull-off force F_{PO}, on the pull-off force enhancement with respect to the static test F_{PO}/F^0_{PO}, on the maximum contact radius that is reached upon vibration activation a_{max} and on the average stress at pull-off σ_{PO}.

Across all experiments and parameters combination, the activation of the base microvibrations produced a characteristic sudden expansion of the contact area, with the amount of increase depending on the test parameters. Upon unloading, the pull-off force F_{PO} initially increases with the vibration amplitude X_b, then suddenly drops at higher X_b. In all the tests, the F_{PO} decay coincided with the onset of radial surface instabilities (surface wrinkles), a nonlinear phenomenon that we identify as the primary mechanism responsible for adhesion degradation in vibroadhesive contacts. Regardless of the substrate thickness t and sphere radius R, the maximum enhancement of the pull-off force relative to the static test remained within the range $F_{PO}/F^0_{PO} \cong 11-13$. Conversely, $\{t, R\}$ strongly influence the range of vibration amplitudes over which adhesion enhancement is sustained: smaller values of t and R providing higher adhesion enhancement F_{PO}/F^0_{PO} for a given X_b. The mean stress at pull-off, σ_{PO}, was generally found in the range $50-100$ kPa, with the exception of the smallest indenter radius ($R = 13.1$ mm), which reached $\sigma_{PO} \cong 186$ kPa. This suggests the feasibility of designing miniaturized adhesive pads with appreciable adhesive performance.

In our experiments, PDMS formulations with base to crosslink weight ratio 5:1, 10:1 and 20:1 were employed. In absolute terms, softer substrates exhibited higher pull-off forces, nevertheless this increase was accompanied by a substantially larger contact area, resulting in a lower average stress at pull-off for the softest formulation (20:1). The base to crosslink ratio strongly affects the range of vibration amplitudes that sustain adhesion amplification. In particular, the stiffest PDMS 5:1 showed a peak in adhesion force already at $X_b = 20$ μm and a vanishing adhesion force at $X_b = 40$ μm, qualitatively resembling the behavior of thin substrates. Preload and unloading rate were found to have no significant influence on the pull-off force. However, in terms of enhancement F_{PO}/F^0_{PO}, higher unloading rates increase the static pull-off force F^0_{PO}, thereby reducing the relative amplification achievable through microvibrations.

It is worth highlighting that, due to the substrate vibrations, the indentation depth can be decomposed into a mean value $\bar{\delta}$ and an oscillating component δ_A. Previous work (Tricarico et al., 2025) has shown that, when the excitation frequency is much larger than the resonance frequency of the indenter (as in the present setup), the

oscillating component satisfies $\delta_A \approx X_b$. The mean indentation $\overline{\delta}$ can be estimated using the JKR model (Johnson et al., 1971). As an example, let us consider the pull-off condition. In load control, the indentation at pull-off is given by:

$$\overline{\delta}_{PO} = (3\pi^2)^{\frac{1}{3}} \frac{R}{4} \left(\frac{\Delta\gamma_{eff}}{E^*_{eff} R} \right)^{\frac{2}{3}} \tag{5}$$

Using a representative parameter set from our experiments (i.e., PDMS 10:1, $t = 5$ mm and $R = 51.5$ mm, $E^*_{eff} = 4.5$ MPa (Tricarico et al., 2025), and $\Delta\gamma_{eff} = 202 \times [2, 6, 12, 14]$ mJ/m^2, corresponding to $X_b = [20, 40, 60, 80]$ μ m, see Fig. 3b) we obtain $\overline{\delta}_{PO} = [5.8, 12.0, 19.1, 21.1]$ μm. This yields a nearly constant ratio $X_b / \overline{\delta}_{PO} \cong \delta_A / \overline{\delta}_{PO} \approx 3.4$ across the explored range. This analysis suggests that, in vibroadhesion problems, the externally imposed oscillatory component of the indentation depth dominates over its mean value.

Furthermore, we showed how a simplified numerical model introduced earlier in Ref (Tricarico et al., 2025). qualitatively reproduces most of the observed experimental trends, within the regime where the material response can be reasonably approximated as linear (PDMS 10:1 behaves linearly up to strains of about 40% (Pal and Bhattacharyya, 2025)). Viscoelasticity is incorporated through the Gent–Schultz power-law relation, which introduces a rate-dependent effective work of adhesion. However, the model does not capture nonlinear effects such as interfacial instabilities (e.g., wrinkle formation) or finite-thickness effects, which become relevant at larger vibration amplitudes. A more accurate description of these regimes would require advanced constitutive models (e.g., hyperelasticity (Lin et al., 2009) and large deformations (Ceglie et al., 2025)) and is left for future work. Despite these limitations, the model successfully captures the main qualitative trends and provides a useful framework for interpreting the results and guiding the design and optimization of vibroadhesive systems.

6. Conclusions

In summary, we conclude that the primary parameters governing the adhesive performance of a vibroadhesive pad are the material properties ($E^*_0, \Delta\gamma_0$), the substrate thickness t and the radius of the indenter R, while preload F_{c0} and unloading rate r play a secondary role. For the design of more efficient vibroadhesive interfaces, thin layers offer the significant advantage of achieving adhesion amplification comparable to thicker substrates at substantially lower vibration amplitudes, which can be exploited to reduce energy consumption of the vibration-modulated interface. Stiffer materials provide a similar advantage, albeit at the cost of a marked reduction in the maximum attainable adhesion force. Overall, this study provides both physical insights and practical guidelines for designing vibroadhesive interfaces through geometrical and material properties, paving the way for the development of actively controllable adhesive systems and advanced gripping devices.

CRediT authorship contribution statement

M. Tricarico: Writing – original draft, Visualization, Methodology, Investigation, Formal analysis, Data curation, Conceptualization. **A.Y. Shiferaw:** Writing – review & editing, Software, Methodology, Investigation, Data curation. **A. Papangelo:** Writing – review & editing, Supervision, Resources, Project administration, Methodology, Funding acquisition, Conceptualization.

Declaration of competing interest

The authors declare that they have no known competing financial interests or personal relationships that could have appeared to influence the work reported in this paper.

Acknowledgment

All authors were partly supported by the Italian Ministry of University and Research under the Program “Department of Excellence” Legge 232/2016 (Grant No. CUP - D93C23000100001). All authors were supported by the European Union (ERC-2021-STG, “Towards Future Interfaces With Tuneable Adhesion By Dynamic Excitation” - SURFACE, Project ID: 101039198, CUP: D95F22000430006). Views and opinions expressed are however those of the authors only and do not necessarily reflect those of the European Union or the European Research Council. Neither the European Union nor the granting authority can be held responsible for them.

Appendix A. Supplementary data

Supplementary data to this article can be found online at https://doi.org/10.1016/j.euromechsol.2026.106130.

Data availability

All the dataset is openly available on Zenodo at DOI: https://doi.org/10.5281/zenodo.19221913.

References

Afferrante, L., Violano, G., 2022. On the effective surface energy in viscoelastic Hertzian contacts. J. Mech. Phys. Solid. 158, 104669. https://doi.org/10.1016/j.jmps.2021.104669.

Argatov, I., Papangelo, A., Ciavarella, M., 2025. An asymptotic model of vibroadhesion. Int. J. Non Lin. Mech. 174, 105089. https://doi.org/10.1016/j.ijnonlinmec.2025.105089.

Autumn, K., Peattie, A.M., 2002. Mechanisms of adhesion in geckos. Integr. Comp. Biol. 42, 1081–1090. https://doi.org/10.1093/icb/42.6.1081.

Bae, W.G., Kim, D., Kwak, M.K., Ha, L., Kang, S.M., Suh, K.Y., 2013. Enhanced skin adhesive patch with modulus-tunable composite micropillars. Adv. Healthcare Mater. 2, 109–113. https://doi.org/10.1002/adhm.201200098.

Carbone, G., Pierro, E., Gorb, S.N., 2011. Origin of the superior adhesive performance of mushroom-shaped microstructured surfaces. Soft Matter 7, 5545–5552. https://doi.org/10.1039/c0sm01482f.

Caruso, F., Shea, H., Cacucciolo, V., 2025. Electroadhesion suction cups. Adv. Mater. 37. https://doi.org/10.1002/adma.202420231.

Ceglie, M., Violano, G., Afferrante, L., Menga, N., 2025. Finite deformations induce friction hysteresis in normal wavy contacts. Int. J. Mech. Sci. 291–292, 110115. https://doi.org/10.1016/j.ijmecsci.2025.110115.

Chen, J., Chen, W., Zhao, M., Jiang, X., Zhu, X., Xu, X., Zhao, J., Tang, Y., Gorb, S.N., Ji, K., Dai, Z., 2025. Ultrafast adhesion/friction bidirectionally switchable control by vibration. Adv. Funct. Mater. https://doi.org/10.1002/adfm.202516421.

Ciavarella, M., Tricarico, M., Papangelo, A., 2025. On the dynamic JKR adhesion problem. Mech. Mater. 202, 105252. https://doi.org/10.1016/j.mechmat.2025.105252.

Delplanque, E., Aymard, A., Dalmas, D., Scheibert, J., 2022. Solving curing-protocol-dependent shape errors in PDMS replication. J. Micromech. Microeng. 32, 045006. https://doi.org/10.1088/1361-6439/ac56ea.

Drotlef, D., Blümler, P., del Campo, A., 2014. Magnetically actuated patterns for bioinspired reversible adhesion (dry and wet). Adv. Mater. 26, 775–779. https://doi.org/10.1002/adma.201303087.

Duan, W., Yu, Z., Cui, W., Zhang, Z., Zhang, W., Tian, Y., 2023. Bio-inspired switchable soft adhesion for the boost of adhesive surfaces and robotics applications: a brief review. Adv. Colloid Interface Sci. 313, 102862. https://doi.org/10.1016/j.cis.2023.102862.

Gent, A.N., Schultz, J., 1972. Effect of wetting liquids on the strength of adhesion of viscoelastic material. J. Adhes. 3, 281–294. https://doi.org/10.1080/00218467208072199.

Greenwood, J.A., Johnson, K.L., 1981. The mechanics of adhesion of viscoelastic solids. Philos. Mag. A 43, 697–711. https://doi.org/10.1080/01418618108240402.

Greiner, C., Spolenak, R., Arzt, E., 2009. Adhesion design maps for fibrillar adhesives: the effect of shape. Acta Biomater. 5, 597–606. https://doi.org/10.1016/j.actbio.2008.09.006.

Hensel, R., Moh, K., Arzt, E., 2018. Engineering micropatterned dry adhesives: from contact theory to handling applications. Adv. Funct. Mater. 28. https://doi.org/10.1002/adfm.201800865.

Johannes, K., Calahan, K., Bowen, L., Zuetell, E., Long, R., Rentschler, M., 2022. Mechanically switchable micro-patterned adhesive for soft material applications. Extreme Mech. Lett. 52, 101622. https://doi.org/10.1016/j.eml.2022.101622.

Johnson, K.L., Kendall, K., Roberts, A.D., 1971. Surface energy and the contact of elastic solids. Proceedings of the Royal Society of London. A. Mathematical and Physical Sciences 324, 301–313. https://doi.org/10.1098/rspa.1971.0141.

Lin, D.C., Shreiber, D.I., Dimitriadis, E.K., Horkay, F., 2009. Spherical indentation of soft matter beyond the Hertzian regime: numerical and experimental validation of hyperelastic models. Biomech. Model. Mechanobiol. 8, 345–358. https://doi.org/10.1007/s10237-008-0139-9.

Linghu, C., Liu, Y., Yang, X., Li, D., Tan, Y.Y., Bin Mohamed Hafiz, M.H., Bin Rohani, M. F., Du, Z., Su, J., Li, Y., Huo, Y., Xu, H., Wang, X., Wang, Y., Yu, J., Gao, H., Hsia, K. J., 2024. Fibrillar adhesives with unprecedented adhesion strength, switchability and scalability. Natl. Sci. Rev. 11. https://doi.org/10.1093/nsr/nwae106.

Linghu, C., Liu, Y., Yang, X., Chen, Z., Feng, J., Zhang, Y., Li, Y., Zhao, Z., Seo, Y.-J., Li, J., Jiang, H., Su, J., Fang, Y., Li, Y., Wang, X., Wang, Y., Gao, H., Hsia, K.J., 2025. Versatile adhesive skin enhances robotic interactions with the environment. Sci. Adv. 11. https://doi.org/10.1126/sciadv.adt4765.

Liu, Z., Yan, F., 2022. Switchable adhesion: On-demand bonding and debonding. Adv. Sci. 9, 2200264. https://doi.org/10.1002/advs.202200264.

Liu, B., Yin, T., Zhu, J., Zhao, D., Yu, H., Qu, S., Yang, W., 2023. Tough and fatigue-resistant polymer networks by crack tip softening. Proc. Natl. Acad. Sci. 120. https://doi.org/10.1073/pnas.2217781120.

Maghami, A., Wang, Q., Tricarico, M., Ciavarella, M., Li, Q., Papangelo, A., 2024a. Bulk and fracture process zone contribution to the rate-dependent adhesion amplification in viscoelastic broad-band materials. J. Mech. Phys. Solid. 193, 105844. https://doi.org/10.1016/j.jmps.2024.105844.

Maghami, A., Wang, Q., Tricarico, M., Ciavarella, M., Li, Q., Papangelo, A., 2024b. Bulk and fracture process zone contribution to the rate-dependent adhesion amplification in viscoelastic broad-band materials. J. Mech. Phys. Solid. 193, 105844. https://doi.org/10.1016/j.jmps.2024.105844.

Narkar, A.R., Kendrick, C., Bellur, K., Leftwich, T., Zhang, Z., Lee, B.P., 2019. Rapidly responsive smart adhesive-coated micropillars utilizing catechol–boronate complexation chemistry. Soft Matter 15, 5474–5482. https://doi.org/10.1039/C9SM00649D.

Pal, S., Bhattacharyya, A., 2025. Measurement of axial and shear mechanical response of PDMS elastomers and determination of Poisson's ratio using digital image correlation. Polym. Test. 143, 108687. https://doi.org/10.1016/j.polymertesting.2025.108687.

Peisker, H., Michels, J., Gorb, S.N., 2013. Evidence for a material gradient in the adhesive tarsal setae of the ladybird beetle Coccinella septempunctata. Nat. Commun. 4, 1661. https://doi.org/10.1038/ncomms2576.

Persson, B.N.J., Brener, E.A., 2005. Crack propagation in viscoelastic solids. Phys. Rev. E 71, 036123. https://doi.org/10.1103/PhysRevE.71.036123.

Schapery, R.A., 1975. A theory of crack initiation and growth in viscoelastic media. Int. J. Fract. 11, 141–159. https://doi.org/10.1007/BF00034721.

Shintake, J., Cacucciolo, V., Floreano, D., Shea, H., 2018. Soft robotic grippers. Adv. Mater. 30, 1707035. https://doi.org/10.1002/adma.201707035.

Shui, L., Jia, L., Li, H., Guo, J., Guo, Z., Liu, Y., Liu, Z., Chen, X., 2020. Rapid and continuous regulating adhesion strength by mechanical micro-vibration. Nat. Commun. 11, 1583. https://doi.org/10.1038/s41467-020-15447-x.

Tan, Y.L., Wong, Y.J., Ong, N.W.X., Leow, Y., Wong, J.H.M., Boo, Y.J., Goh, R., Loh, X.J., 2024. Adhesion evolution: designing smart polymeric adhesive systems with On-Demand reversible switchability. ACS Nano 18, 24682–24704. https://doi.org/10.1021/acsnano.4c05598.

Tang, Y., Goodarzi, F., Wan, G., Shan, W., 2025. Pick-and-Place grippers with tunable adhesion from capped soft hollow pillar structure. Adv. Mater. Technol. 10. https://doi.org/10.1002/admt.202500216.

Tricarico, M., Ciavarella, M., Papangelo, A., 2025. Enhancement of adhesion strength through microvibrations: modeling and experiments. J. Mech. Phys. Solid. 196, 106020. https://doi.org/10.1016/j.jmps.2024.106020.

Violano, G., Afferrante, L., 2022. Size effects in adhesive contacts of viscoelastic media. Eur. J. Mech. Solid. 96, 104665. https://doi.org/10.1016/j.euromechsol.2022.104665.

Violano, G., Chateauminois, A., Afferrante, L., 2021. Rate-dependent adhesion of viscoelastic contacts, Part I: contact area and contact line velocity within model randomly rough surfaces. Mech. Mater. 160, 103926. https://doi.org/10.1016/j.mechmat.2021.103926.

Wang, Y., Zhang, X., Hensel, R., Arzt, E., 2022. Sliding mechanism for release of superlight objects from micropatterned adhesives. Adv. Mater. Interfac. 9. https://doi.org/10.1002/admi.202101764.

Wang, Q., Papangelo, A., Ciavarella, M., Gao, H., Li, Q., 2025. Rapid detachment of a rigid sphere adhered to a viscoelastic substrate: an upper bound model incorporating Maugis parameter and preload effects. J. Mech. Phys. Solid. 196, 106028. https://doi.org/10.1016/j.jmps.2025.106028.

Yi, J., Haouas, W., Gauthier, M., Rabenorosoa, K., 2024. A PDMS/silicon adhesion control method at millimeter-scale based on microvibration. Advanced Intelligent Systems n/a, 2400394. https://doi.org/10.1002/aisy.202400394.

Zhang, X., Wang, Y., Tian, Z., Samri, M., Moh, K., McMeeking, R.M., Hensel, R., Arzt, E., 2022. A bioinspired snap-through metastructure for manipulating micro-objects. Sci. Adv. 8. https://doi.org/10.1126/sciadv.add4768 eadd4768.

Zhao, J., Li, X., Tan, Y., Liu, X., Lu, T., Shi, M., 2022. Smart adhesives via magnetic actuation. Adv. Mater. 34, e2107748. https://doi.org/10.1002/adma.202107748.